RSC Advances

ROYAL SOCIETY OF CHEMISTRY

PAPER

View Article Online
View Journal | View Issue

Check for updates

Cite this: *RSC Adv.*, 2020, **10**, 27456

# The dielectric relaxation behavior induced by sodium migration in the $Na_2CoSiO_4$ structure within a three-dimensional Co–O–Si framework

Kawthar Trabelsi,[a] Karim Karoui,[a] Abdelfattah Mahmoud,[b] Jérôme Bodart,[b] Frédéric Boschini[b] and Abdallah Ben Rhaiem *[a]

Received 4th June 2020
Accepted 14th July 2020

DOI: 10.1039/d0ra04912c

rsc.li/rsc-advances

The disodium cobalt(II) orthosilicate material (NCS) has been synthesized using improved solid-state (NCS-SS) and co-precipitation (NCS-CP) methods of synthesis. The Rietveld refinement of the XRD pattern of $Na_2CoSiO_4$ has demonstrated an orthorhombic crystal system with the space groups $Pna2_1$ and $Pbca$ for NCS-SS and NCS-CP respectively. The elemental mapping of microstructures by scanning electron microscopy-energy dispersive spectroscopy (SEM-EDS) showed the porous morphology and the homogenous particles of the $Na_2CoSiO_4$ powders. Their dielectric properties were measured in the frequency and temperature ranges of 0.1–$10^6$ Hz and 383–613 K respectively. Different dielectric relaxation phenomena associated with the $Na^+$-ion migration through different paths were displayed in relation with the temperature and frequency. The decrease and increase in the dielectric properties were found to be dependent on the formation of short-range ordered structure formed after the migration of $Na^+$-ions. In the present work, an attempt has been made to study the relation between the structural properties and the dielectric process. Thus, interesting insights into the transport behavior of $Na^+$-ions in different chemical environments were obtained. This in turn provides an effective procedure to probe the relationship between the diffusion pathway of $Na^+$-ions and the dielectric response.

## 1. Introduction

Recently, considerable attention has been paid to Na-ion batteries (NIBs) with high energy density, low price and toxicity, relatively low self-discharge, good chemical stability, good mechanical stability and dielectric properties.[1–5] Additionally, sodium is located below lithium in the periodic table, thus, such physical and chemical properties as ionic charge, electronegativity and electrochemical reactivity are very similar,[6–8] which makes NIBs an attractive alternative to lithium-ion batteries (LIBs). More importantly, there are large numbers of resources of Na and Si in the Earth's crust. $Na_2CoSiO_4$ exhibits significantly lower polarization than $Na_2FeSiO_4$ and $Na_2MnSiO_4$. Much like $Li_2CoSiO_4$, sodium cobalt-based orthosilicate ($Na_2CoSiO_4$) tends to be a good choice to serve as the cathode material in NIBs.[9] WU Shun-qing *et al.*[10] proved that changing the amount of Na in $Li_2CoSiO_4$ has a great influence on the structural properties. More precisely, this change is due to the presence of sodium and the distortion of its local environment, especially the $SiO_4$ and $CoO_4$ tetrahedra. Accordingly, we can notice that the sodium-ion migration and its environment are responsible for the physical proprieties which are significant for the cathode materials.[11,12] The polymorphism of the cristobalite is porous while the arrangement of the transition metal silicate brings about large tunneling sites that can incorporate the diffusion of the cations.[13,14] Disodium cobalt orthosilicate has attractive properties such as a high structural stability, a high $Na^+$ diffusion of $8.0 \times 10^{-12}$ cm$^2$ s$^{-1}$ at 300 K (ref. 15) and a good electrical conductivity which is reported to be purely ionic.[16] The $Na^+$ diffusion indicates a very low activation barrier and a 3D network of diffusion pathways through the $SiO_4$ and $MO_4$ frameworks,[17] which both suggest favorable $Na^+$ intercalation kinetics.

The dielectric permittivity, the dielectric loss and the electric modulus must be carried out in order to demonstrate the migration of sodium-ion in broad temperature and frequency ranges as well as to obtain a better understanding of the relaxation mechanism. Nevertheless, only few researchers have studied the dielectric properties of electrodes.

Finding a relationship between the composition, the structure and the dielectric properties should be of considerable interest. Therefore, the aim of this work is (a) to reexamine the structure of $Na_2CoSiO_4$ by the improved solid-state and co-precipitation methods, (b) to discuss its crystal chemical characteristics and its microstructure morphologies, and (c) to investigate the relaxation behavior of the $Na^+$-ion migration as a function of the temperature, the frequency and the synthesis methods.

---

[a] *Laboratory LaSCOM, University of Sfax, BP1171, 3000, Sfax, Tunisia. E-mail: abdallahrhaiem@yahoo.fr*

[b] *GREENMAT, CESAM, Institute of Chemistry B6, University of Liège, 4000 Liège, Belgium*

# 2. Experimental

### 2.1. Synthesis of $Na_2CoSiO_4$

In this work, the $Na_2CoSiO_4$ (NCS) material was prepared through the improved solid-state (NCS-SS) and co-precipitation (NCS-CP) methods.

The $Na_2CoSiO_4$ (NCS-SS) was synthesized for the first time by the improved solid-state method. The reaction scheme was the following:

$$6Na_2CO_3 + 6SiO_2 + 2Co_3O_4 \rightarrow 6Na_2CoSiO_4 + 6CO_2 + O_2 \quad (1)$$

$Na_2CO_3$ and $Co_3O_4$ were used as starting materials for sodium and cobalt sources respectively. $Na_2CO_3$ (Sigma-Aldrich, 99%) and $Co_3O_4$ (Sigma-Aldrich > 97%) were first mixed in ethanol under magnetic stirring at 50 °C for 5 hours. Then, the silicon source ($SiO_2$) (Sigma-Aldrich, 99.9%, 0.5–10 μm) was added to the suspension. The temperature increased to 80 °C to evaporate the ethanol and the water. Next, a few drops of nitric acid were slowly added to the above mixture. After that, a homogeneous suspension was formed and kept stirring until it yielded the mixed precursor. The resulting suspension was dried at 350 °C for 12 h to avoid ambient moisture and gases, especially $CO_2$ evaporation. The grey powder was sintered at 900 °C for 9 hours under an argon atmosphere to avoid contact with humid air and to form the blue NCS-SS sample. On the other hand, $Na_2CoSiO_4$ was prepared according to the synthesis protocol shown by Joshua Treacher *et al.*[15] using the co-precipitation synthesis route. NaOH (Sigma-Aldrich > 98%), $CoCl_2$ (Sigma-Aldrich > 98%) were used as sodium and cobalt sources and TEOS (tetraethylorthosilicate) (Sigma-Aldrich, 98%) as a silicon source. The resulting dry residues were washed with ethanol and distilled water to remove the presence of $Cl^-$. The blue precipitate was dried at 80 °C for 12 h. The prepared powder was sintered eventually at 600 °C for 8 h under an argon atmosphere to obtain the NCS-CP material.

### 2.2. Characterization techniques

The phase formation was identified by the X-ray powder diffraction technique using Bruker D8 Discover Twin-Twin with an advance diffractometer in Bragg–Brentano geometry with Cu K$\alpha$ radiation ($\lambda = 1.5406$ Å, $10° \leq 2\theta \leq 90°$). Refinements were carried out using the FullProf program based on the Rietveld method.[18] To investigate the morphology of the prepared samples, the scanning electron microscope (XL30 FEG ESEM, FEI) was used with an accelerating voltage of 15 kV under high vacuum. Dielectric impedance measurements were determined using the double platinum electrode configuration of Solartron SI-1260 in the frequency range of 0.1–$10^6$ Hz and the 383–613 K temperature range.

# 3. Results and discussions

### 3.1. X-ray diffractions

The refinement results of X-ray diffraction patterns of the synthesized $Na_2CoSiO_4$ (NCS-SS and NCS-CP) at room temperature are shown in Fig. 1(a) and (b) for NCS-SS and NCS-CP. The Rietveld refinement results are in agreement with the previously reported data.[15] The small difference between the calculated/experimental patterns and the low values of the agreement parameters confirms the successful refinement of the experimental data. The main X-ray diffraction peaks were assigned to the $Na_2CoSiO_4$ material for the two samples. In addition, the peaks were sharp indicating the high degree of crystallinity of the synthesized NCS samples.

Overall, Na/Li orthosilicate materials were indexed in primitive systems.[19] NCS-SS was indexed successfully on the basis of an orthorhombic unit cell with the $Pna2_1$ space group. The corresponding cell parameters obtained from the data are as follows: $a = 10.9549(7)$ Å, $b = 5.2523(3)$ Å, $c = 7.0440(6)$ Å, $\alpha = \beta = \gamma = 90°$, $V = 405.29(5)$ Å$^3$ and $Z = 4$ with a reliability factor of $\chi^2 = 1.8$. The small peaks correspond to the impurity phase δ-$Na_2Si_2O_5$ (3.6%).[20] While NCS-CP has the same orthorhombic crystal structure, its space group is *Pbca* and its cell parameters correspond to: $a = 10.3176\ (2)$ Å, $b = 14.6019\ (7)$ Å, $c = 5.1558\ (2)$ Å, V = 771.85(3) Å$^3$ and $Z = 8$ with a reliability factor of $\chi^2 = 1.48$. Based on the refinement, the relative amount of the NCS-CP phase is 96.88%. However, the relative amount of the γ-$Na_2Si_2O_5$ impurity is 3.18%. $Na_2Si_2O_5$ is frequently the minority impurity in the NCS compounds. The refined structural parameters of NCS-SS and NCS-CP and their impurities are summarized in Table 1. Both factors $R_{wp}$ and $R_B$ which are the fit factors are reasonably small, indicating that the phases of sodium orthosilicate are appropriate structural models for

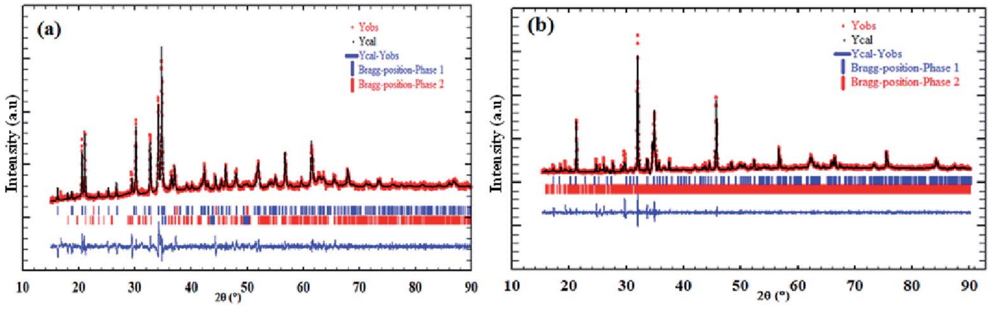

Fig. 1 Graphical results of the Rietveld refinement of synthesized $Na_2CoSiO_4$ by (a) ameliorate solid state method denoted NCS-SS, (b) co-precipitation method denoted NCS-CP.

Table 1 Crystal data of the $Na_2CoSiO_4$ compound and the detected impurities

| Formula | NCS-SS | δ-$Na_2Si_2O_5$ | NCS-CP | γ-$Na_2Si_2O_5$ |
|---|---|---|---|---|
| Crystal system | Orthorhombic | Monoclinic | Orthorhombic | Monoclinic |
| Space group | $Pna2_1$ | $P12_1/c_1$ | $Pbca$ | $C12/c_1$ |
| Formula units (Å) | $a = 10.9549(7)$ | $a = 8.3993(2)$ | $a = 10.3176(2)$ | $a = 33.3766(11)$ |
| | $b = 5.2523(3)$ | $b = 12.083(3)$ | $b = 14.6019(7)$ | $b = 14.0877(5)$ |
| | $c = 7.0440(6)$ | $c = 4.843(1)$ | $c = 5.1558(2)$ | $c = 26.1507(7)$ |
| | $\alpha = \beta = \gamma = 90°$ | $\alpha = \gamma = 90°, \beta = 90.37(3)$ | $\alpha = \beta = \gamma = 90°$ | $\alpha = \gamma = 90°, \beta = 108.60°$ |
| $R_p$ (%) | 27.6 | 27.6 | 25.6 | 25.6 |
| $R_{wp}$ (%) | 25.6 | 25.6 | 23.6 | 23.6 |
| $R_{exp}$ (%) | 19.10 | 19.10 | 19.37 | 19.37 |
| $R_B$ | 3.462 | 2.245 | 2.384 | 3.129 |
| $R_f$ | 2.679 | 2.046 | 2.047 | 3.117 |
| $\chi^2$ | 1.79 | 1.79 | 1.48 | 1.48 |
| % | 96.4 | 3.6 | 96.88 | 3.18 |

$Na_2CoSiO_4$. The final atomic coordinates and the isotropic displacement parameters are listed in Table 2, while the bond angles and distances are given in Tables 3 and 4.

### 3.2. Description of the NCS structures

$Na_2MSiO_4$ (M = Fe, Mn, Co) is classified among the C-type compounds. It crystallized in the three-dimensional (3D) frameworks of the $CoO_4$ and $SiO_4$ tetrahedral units.[21] The structure of $Na_2CoSiO_4$ deviated from the orthorhombic arrangement because of the different sizes of the Na, Co and Si atoms and their tetrahedral coordination. The powder pattern of $Na_2CoSiO_4$ indicates that it is isostructural with the $Na_2BeSiO_4$ structure.[22,23]

The structure can be considered as a 'stuffed' cristobalite with corner-sharing alternate transition metal and silicon tetrahedral units. In general, the orthosilicates are characterized by tetrahedral anion units, in particular $(SiO_4)^{4-}$, covalently bonded to the $MO_4$ polyhedra.[24,25] The relative orientation of the tetrahedra and the degree of corrugation in the layers differ considerably according to the modification.

Table 2 Fractional atomic coordinates and equivalent isotropic displacement parameters of $Na_2CoSiO_4$

| Atom | Wyck | $x$ | $y$ | $z$ | $O_{cc}$ |
|---|---|---|---|---|---|
| **NCS-SS** | | | | | |
| Co(1) | 4$a$ | 0.15484 | 0.25746 | 0.63431 | 1 |
| Si(2) | 4$a$ | 0.40688 | 0.26700 | 0.10603 | 1 |
| Na(1) | 4$a$ | 0.17294 | 0.23567 | 0.10603 | 1 |
| Na(2) | 4$a$ | 0.40630 | 0.26710 | 0.36897 | 1 |
| O(1) | 4$a$ | 0.32064 | 0.24200 | 0.69309 | |
| O(2) | 4$a$ | 0.09690 | 0.44781 | 0.40866 | |
| O(3) | 4$a$ | 0.04951 | 0.28720 | 0.88692 | |
| O(4) | 4$a$ | 0.14226 | 0.88014 | 0.57608 | |
| **NCS-CP** | | | | | |
| Co(1) | 8$c$ | 0.97150 | 0.81450 | 0.70095 | 0.5 |
| Si(1) | 8$c$ | 0.97150 | 0.81450 | 0.70095 | 0.5 |
| Co(2) | 8$c$ | 0.26550 | 0.05584 | 0.27810 | 0.5 |
| Si(2) | 8$c$ | 0.26550 | 0.05584 | 0.27810 | 0.5 |
| Na(1) | 8$c$ | 0.48810 | 0.06810 | 0.68160 | 0.5 |
| Na(2) | 8$c$ | 0.50450 | 0.04080 | 0.77420 | 0.5 |
| Na(3) | 8$c$ | 0.74650 | 0.31280 | 0.18090 | 0.5 |
| Na(4) | 8$c$ | 0.79510 | 0.30730 | 0.37460 | 0.5 |
| O(1) | 8$c$ | 0.06560 | 0.91190 | 0.80300 | |
| O(2) | 8$c$ | 0.01920 | 0.78010 | 0.42380 | |
| O(3) | 8$c$ | 0.23960 | 0.95950 | 0.12760 | |
| O(4) | 8$c$ | 0.79130 | 0.83870 | 0.84560 | |

The $Pna2_1$-$Na_2CoSiO_4$ structure can be viewed as a build-up of infinite zig–zag paths alternating $(CoO_4)^{4-}$ and $(SiO_4)^{4-}$ in the ($c$, $b$) plan. These tetrahedra built up a network with channels along the a axis in which the $Na^+$-ions were arranged as represented in Fig. 2(a). In the periodic structure, half the $CoO_4$ and $SiO_4$ tetrahedra pointed along (100), while the other half pointed in the opposite direction (−100) in an alternate manner and were linked only by sharing corners. The mechanism process was induced by the parallel displacement of $Na^+$-ions along the $c$ axis. It consists of double chains of deformed $(CoO_4)^{4-}$ tetrahedra that were parallel-propagated in the ($a$, $c$) plan and interlinked partially by corner-sharing. Each $(SiO_4)^{4-}$ group was thus surrounded by four $(CoO_4)^{4-}$ tetrahedra and *vice versa*, ultimately forming cavities. The average values of the bond lengths of Si–O and Co–O in the $(SiO_4)^{4-}$ and $(CoO_4)^{4-}$ tetrahedra are 1.6465 Å and 2.0025 Å respectively (Table 3). Moreover, it is clear that the average bond lengths of Co–O in $(CoO_4)^{4-}$ tetrahedra were much larger than those of Si–O in the $(SiO_4)^{4-}$ tetrahedra. Na(1) and Na(2) ions occupied the tetrahedral sites located between two $[SiO_4–CoO_4]^{4-}$ layers. Other paths with longer Na–Na hop distances should yield high migration for batteries around 3 Å. Regarding the Na(1) and

Table 3 Selected distances of $Na_2CoSiO_4$ (Å)

| NCS-SS | | NCS-CP | |
|---|---|---|---|
| Bond distances (Å) | | Bond distances (Å) | |
| Co1–O1 | 1.865 | Co1–O4 | 2.034 |
| Co1–O2 | 1.982 | Co1–O1 | 1.801 |
| Co1–O3 | 2.127 | Co1–O2 | 1.863 |
| Co1–O4 | 2.028 | Si1–O2 | 1.593 |
| Si1–O1 | 1.603 | Co2–O1 | 1.810 |
| Si1–O2 | 1.693 | Co2–O3 | 1.817 |
| Si1–O3 | 1.590 | Si2–O4 | 1.767 |
| Si1–O4 | 1.621 | Si2–O3 | 1.629 |

Table 4 Selected angles of $Na_2CoSiO_4$ (°)

| NCS-SS | | NCS-CP | |
|---|---|---|---|
| Atoms (1, 2, 3, 4) | | Atoms (1, 2, 3, 4) with M = Co/Si | |
| O1–Co1–O4 | 93.93 | O2–M1–O4 | 98.29 |
| O3–Si1–O2 | 80.80 | O4–M2–O1 | 96.78 |
| O1–Si1–O2 | 90.78 | O1–M2–O3 | 89.41 |
| Co1–O1–Na2 | 99.34 | O1–Na1–O3 | 69.44 |
| Co1–O2–Na2 | 97.78 | O3–Na1–O1 | 99.74 |
| Co1–O4–Na2 | 95.16 | O4–Na4–O2 | 96.29 |
| Na1–O4–Na2 | 92.28 | M2–O1–Na2 | 92.52 |
| O1–Co1–O3 | 110.24 | M2–O1–Na1 | 94.31 |
| O2–Co1–O4 | 107.99 | M2–O1–Na1 | 88.32 |
| O2–Co1–O3 | 117.40 | M1–O1–Na1 | 75.23 |
| O4–Co1–O3 | 101.78 | M1–O2–Na4 | 86.58 |
| O1–Co1–O2 | 120.79 | M2–O3–Na4 | 82.45 |
| O3–Si1–O1 | 127.11 | M2–O3–Na1 | 93.79 |
| O3–Si1–O4 | 110.48 | Na4–O3–Na1 | 71.28 |
| O1–Si1–O4 | 122.20 | Na3–O3–Na1 | 81.88 |
| O4–Si1–O2 | 103.69 | M1–O3–Na3 | 81.88 |
| O3–Na1–O4 | 119.39 | O2–M1–O1 | 110.16 |
| O4–Na2–O2 | 116.49 | O2–M1–O2 | 103.76 |
| O4–Na2–O1 | 141.68 | O2–M1–O4 | 131.77 |
| O2–Na2–O1 | 101.44 | O1–M1–O2 | 105.25 |
| Si1–O1–Co1 | 138.50 | O1–M1–O4 | 104.39 |
| Si1–O1–Na2 | 120.95 | O3–M2–O4 | 121.76 |
| Si1–O2–Co1 | 128.05 | O3–M2–O1 | 114.62 |
| Si1–O2–Na2 | 115.50 | O3–M2–O3 | 111.18 |
| Si1–O3–Na1 | 130.89 | O4–M2–O3 | 117.13 |
| Si1–O3–Co1 | 118.66 | O1–Na1–O1 | 104.77 |
| Na1–O3–Co1 | 105.06 | O4–Na3–O3 | 102.86 |
| Si1–O4–Co1 | 123.80 | O4–Na3–O4 | 119.65 |
| Si1–O4–Na1 | 105.41 | O3–Na3–O4 | 134.20 |
| Si1–O4–Na2 | 129.24 | O3–Na4–O4 | 147.93 |
| Co1–O4–Na1 | 104.97 | O3–Na4–O2 | 106.07 |
| | | M1–O1–M2 | 134.75 |
| | | M1–O1–Na2 | 120.60 |
| | | M1–O1–Na1 | 104.18 |
| | | M1–O1–Na1 | 125.19 |
| | | M2–O1–Na1 | 106.90 |
| | | M1–O2–M1 | 134.88 |
| | | M1–O2–Na4 | 137.91 |
| | | M2–O3–M2 | 125.72 |
| | | M2–O3–Na4 | 151.79 |
| | | M2–O3–Na3 | 125.03 |
| | | M2–O3–Na1 | 104.50 |
| | | M2–O3–Na3 | 107.73 |
| | | M2–O4–Na3 | 117.06 |
| | | M2–O3–M1 | 108.80 |
| | | M2–O3–Na4 | 134.27 |
| | | M2–O3–Na3 | 128.42 |
| | | Na3–O3–M1 | 120.68 |
| | | M1–O3–Na4 | 102.45 |

Na(2), they were arranged along (100). Moreover, it is very important to note that Na(1) and Na(2) were trapped in two antiparallel cavities ($T_1$ and $T_2$) (Fig. 2(a)). This result would have a great influence on the migration process of $Na^+$-ions.

The *Pbca*-$Na_2CoSiO_4$ is similar to the structure published by J. C. Treacher *et al.*[15] The positions of $Co^{2+}$, $Si^{4+}$ cations in NCS-CP show that silicon and cobalt occupied the same site (Fig. 2(b)). $Na^+$ cations were stuffed onto the vacant tetrahedral sites. All tetrahedra were not oriented in the same way. The results presented here demonstrate that future work should consider how to exploit the importance of cavities. Since the tetrahedra around the Na atoms only shared corners with neighboring Na cavity, and since the tetrahedra of the Si and Co atoms were fully occupied and smaller than the Na tetrahedra, the diffusion of $Na^+$-ions must proceed through the unoccupied tetrahedral sites in the structure. Eventually, forming the parallel and antiparallel cavities ($T_1$, $T_2$) played the main role in the structure and clearly drove the system. In the present work, the different space groups could be expressed either Co and Si sources or the different sintered temperature (900° for NCS-SS and 600° for NCS-CP).

## 3.3. Scanning electron microscopy

Besides the crystallographic structure, the morphological features are important to reinforce and bring out the dielectric mechanism of the material. Thus, we have studied the morphological characteristics of the prepared powders. The SEM micrographs of the NCS-SS and NCS-CP are presented in Fig. 3. The SEM images of the two samples were clearly constituted of an agglomeration of the small particles which led to sub-micrometer particles. This could be due to the relatively high calcination temperature (900 °C) and (600 °C) for NCS-SS and NCS-CP respectively. The measured sizes of the particles are 1.4 μm for NCS-SS and 0.7 μm for NCS-CP. Furthermore, in both $Na_2CoSiO_4$ samples, we could observe the presence of small-sized particles defined as secondary particles. Consequently, the presence of these particles may improve the charge storage through the reduction of migration path lengths.[26] Hence, the formation of micro-sized particles, hollow structure and morphology density are beneficial as electrode material for secondary batteries.[27]

On the other hand, the SEM and EDS link the surface morphology to its chemical composition. The EDS spectra were taken at several points on the surface of the samples. In Fig. 4(a) and (b), the existing elements are illustrated in the EDS spectra. In order to measure the stoichiometry of each element, the EDS analysis was carried out. The individual atoms such as Na, Co and Si were observed in the EDS spectra suggesting homogeneous distribution of the elements. Moreover, the ratios of atoms for Na, Co, Si and O were very close to the stoichiometric ratio of both $Na_2CoSiO_4$ samples which in turn supported the determination of the purity of the $Na_2CoSiO_4$ particles together with the powder XRD. It is interesting to note that $Cl^-$-ion was directly observed with a small percentage in the surface layer of NCS-CP. The result is very close to its theoretical composition ratio 2 : 1 : 1.

## 3.4. Dielectric relaxation

We have adopted the permittivity formalism to study the relaxation mechanism and to explore the ion dynamics in the NCS compounds at different temperatures and frequencies. The real ($\varepsilon'$) and imaginary ($\varepsilon''$) parts of the complex permittivity for NCS-SS and NCS-CP are plotted in Fig. 5(a)–(d) as a function of angular frequency $\omega$ ($\omega = 2\pi f$) at various temperatures. Both $\varepsilon'$

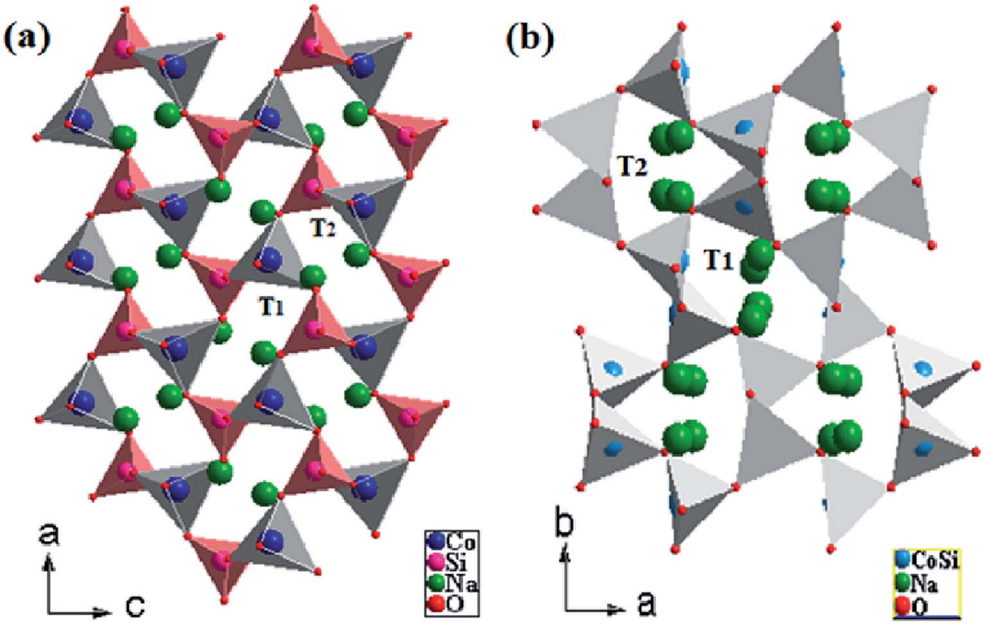

Fig. 2 $Na_2CoSiO_4$ structures as a 'stuffed cristobalite' with corner sharing $CoO_4$ tetrahedra connected *via* $SiO_4$ tetrahedra (a) NCS-SS and (b) NCS-CP.

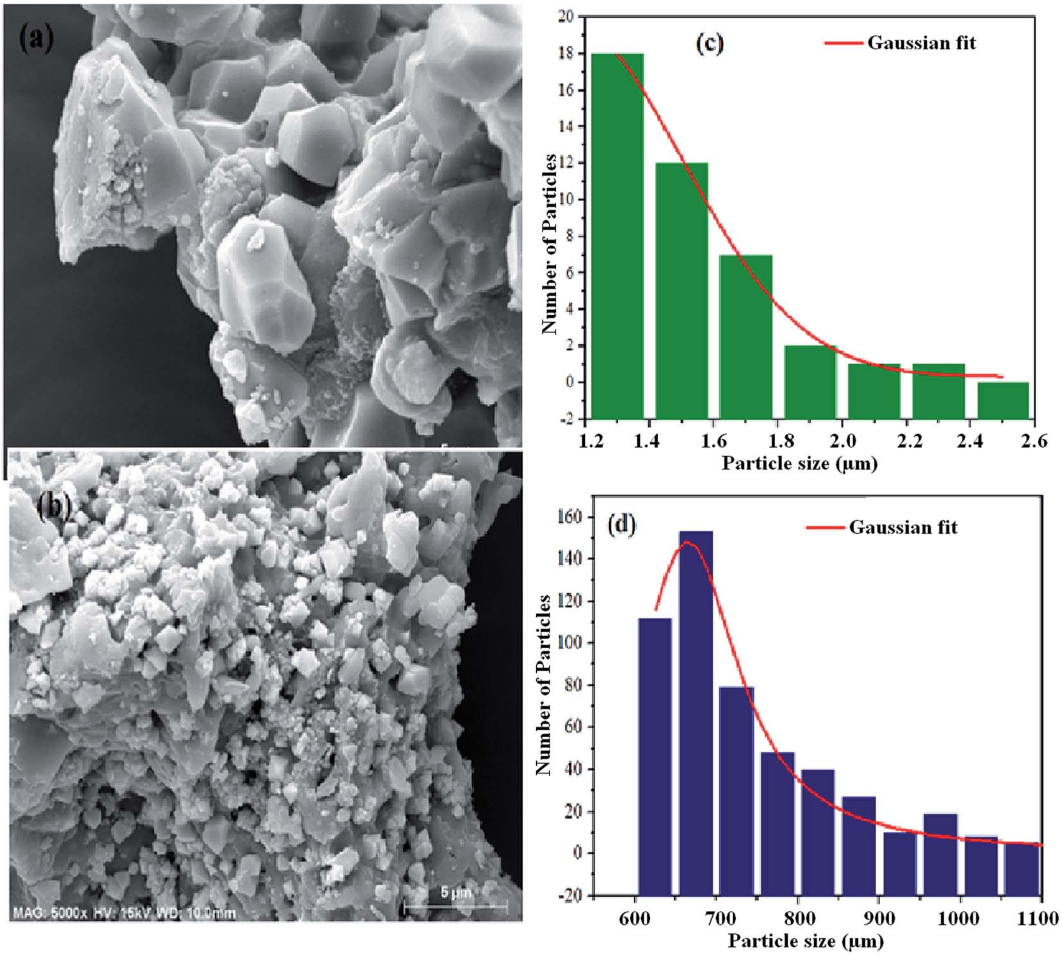

Fig. 3 SEM micrograph of the fractured surface of NCS-SS (a) and NCS-CP (b) samples heat treated at 900 °C and 600 °C under argon. The corresponding particle size histograms (c and d) are presented in the right of the figure.

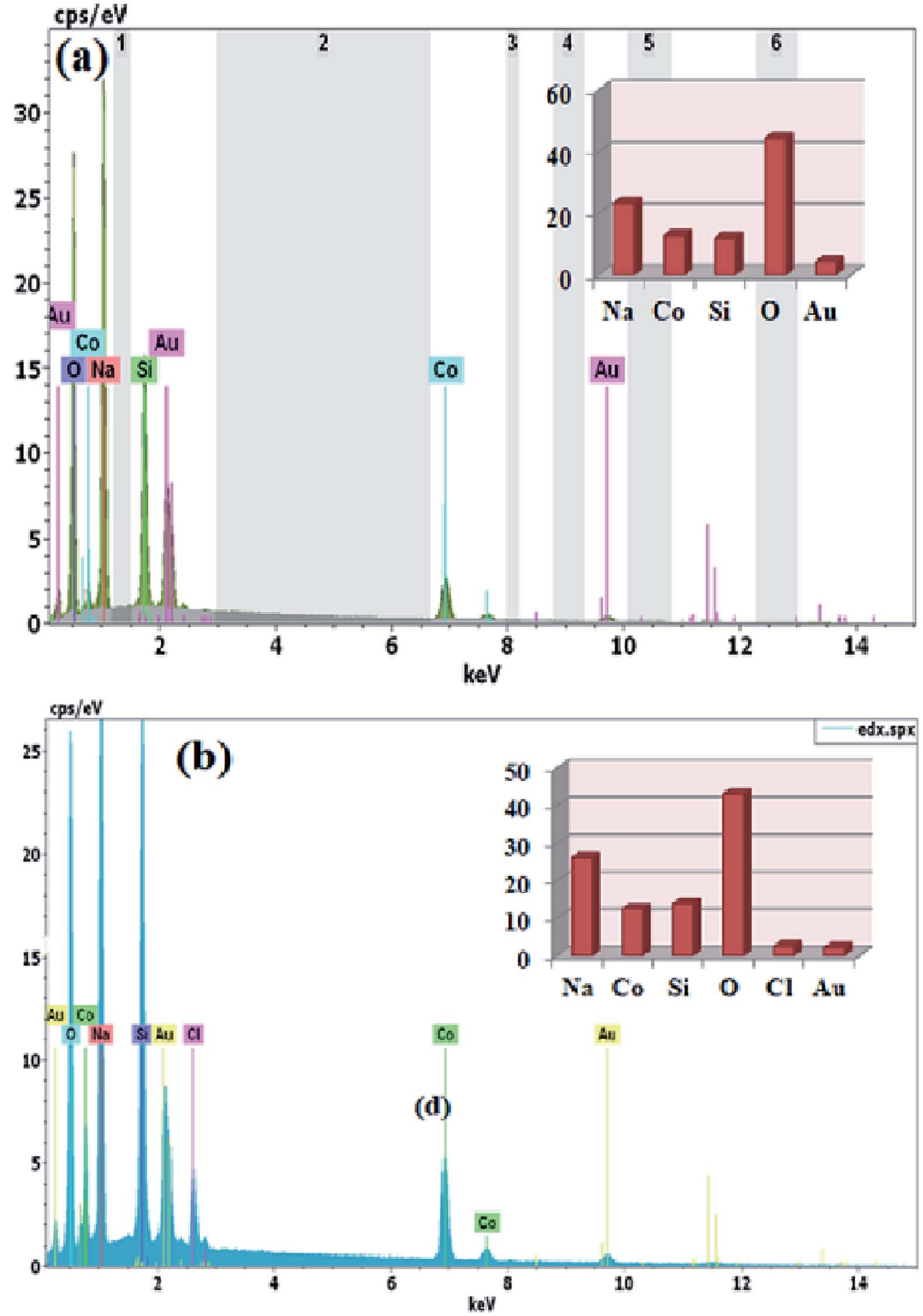

Fig. 4 EDX spectra of the fractured surface of NCS-SS (a) and NCS-CP (b) samples sintered at 900 °C and 600 °C, respectively.

and $\varepsilon''$ attained a minimum value at high frequencies irrespective of the temperature. The mounting value of $\varepsilon'$ with the climb of temperature might be attributed to the rise in the process of space charge polarization. With the increasing frequency (when $\omega < 1/\tau$), dipoles began to lag behind the field and $\varepsilon'$ slightly decreased. When the frequency reached the characteristic frequency ($\omega = 1/\tau$), the dielectric constant dropped and demonstrated the relaxation process. At very high frequencies ($\omega \gg 1/\tau$), dipoles could no longer follow the field. Thus, the increasing value of $\varepsilon'$ in the high and mid frequency regions was associated with the dipolar polarization ($Na^+$-ions). The high values of $\varepsilon'$ at a relatively low frequency might be due to the extrinsic contribution (the space charge localization at NCS). It seems clear that NCS-SS presents three contributions. The two contributions at high and mid frequencies were shown by two types of charge carriers ($Na^+$-ions) which were

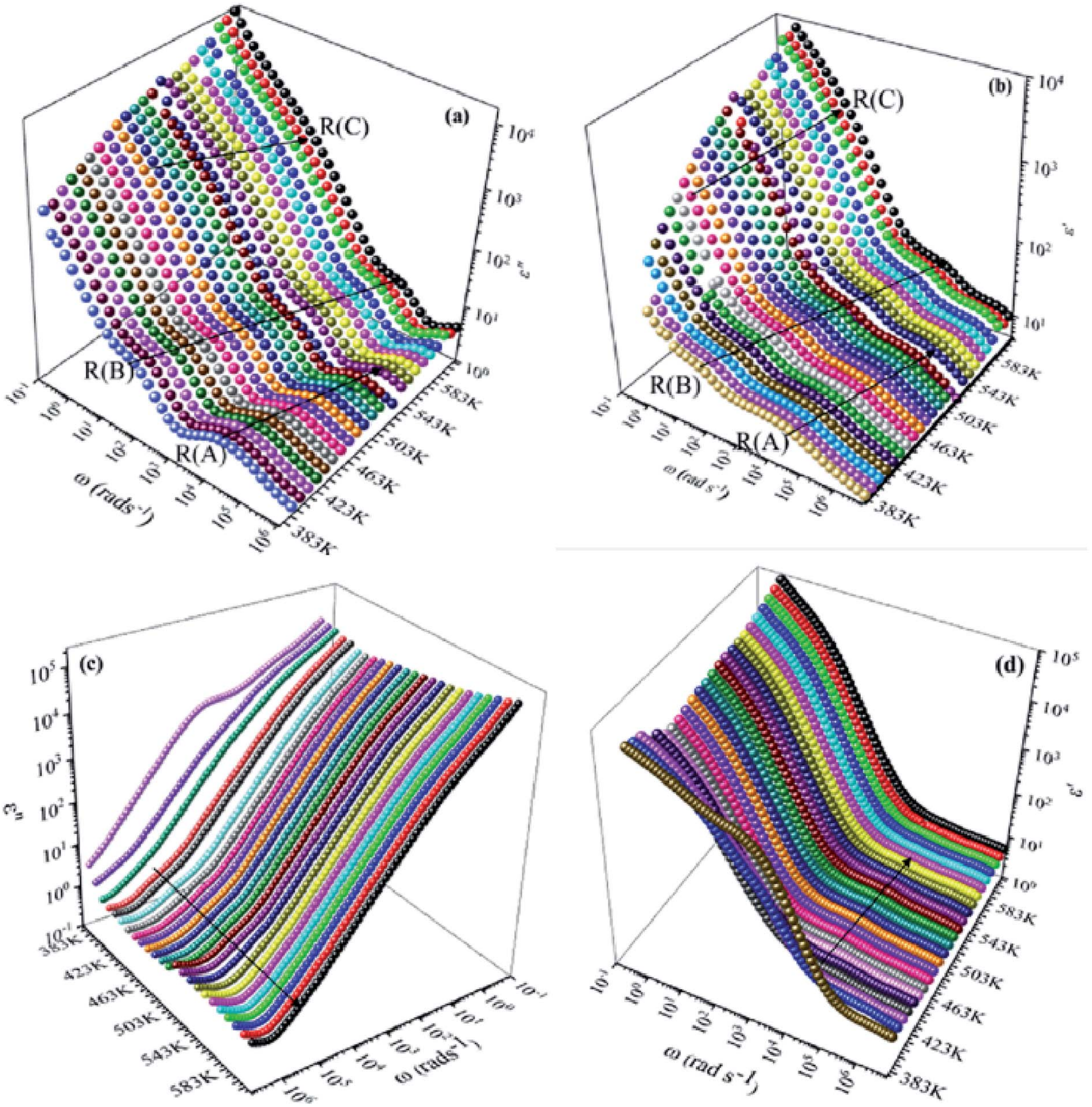

Fig. 5 Dielectric loss $\varepsilon''$ and dielectric constant $\varepsilon'$ as a function of frequency for NCS-SS (a and b) and NCS-CP (c and d) at various temperatures ranging from 383 K to 613 K with the interval of 10 K.

responsible to move only over short distances. This process was in agreement with the existence of two types of cavities in both NCS materials. The third contribution corresponded to the process of space charge polarization at low frequencies. At high frequency, NCS-CP has demonstrated a weak appearance of the relaxation peaks. According to Fig. 5(b) and (d), $\varepsilon''$ increased with mounting temperature, which reveals the dipolar molecular dynamics at high and medium frequency ranges. Typically, the dielectric constant shifted toward high frequencies with the increase in temperature, exhibiting a thermally activated behavior. Moreover, the rise in temperature brought thermal agitation in the compounds, which can produce a deformation cavity.[28] Consequently, the mobility of the ions increased. The corresponding variation of the dielectric loss as a function of the angular frequency has been investigated. Fig. 6(a) and (b) display the tan $\delta$ spectra. We can see that three clear peaks were detected in the frequency dependence of the dielectric loss for NCS-SS and two peaks one of which was too weak to be observed for NCS-CP. For the NCS-SS material, when the temperature climbed, the first relaxation (A) disappeared at high frequencies between $1 \times 10^6$ to $3.8 \times 10^4$ Hz. At mid frequency, the second relaxation (B) between $2.4 \times 10^4$ and $1.4 \times 10^3$ Hz spread to high frequencies when the temperature went up. Meanwhile, the third relaxation (C) appeared at a certain low frequency below 200 Hz and in a high temperature region. Since the relaxation maximum shifted monotonically to low temperatures

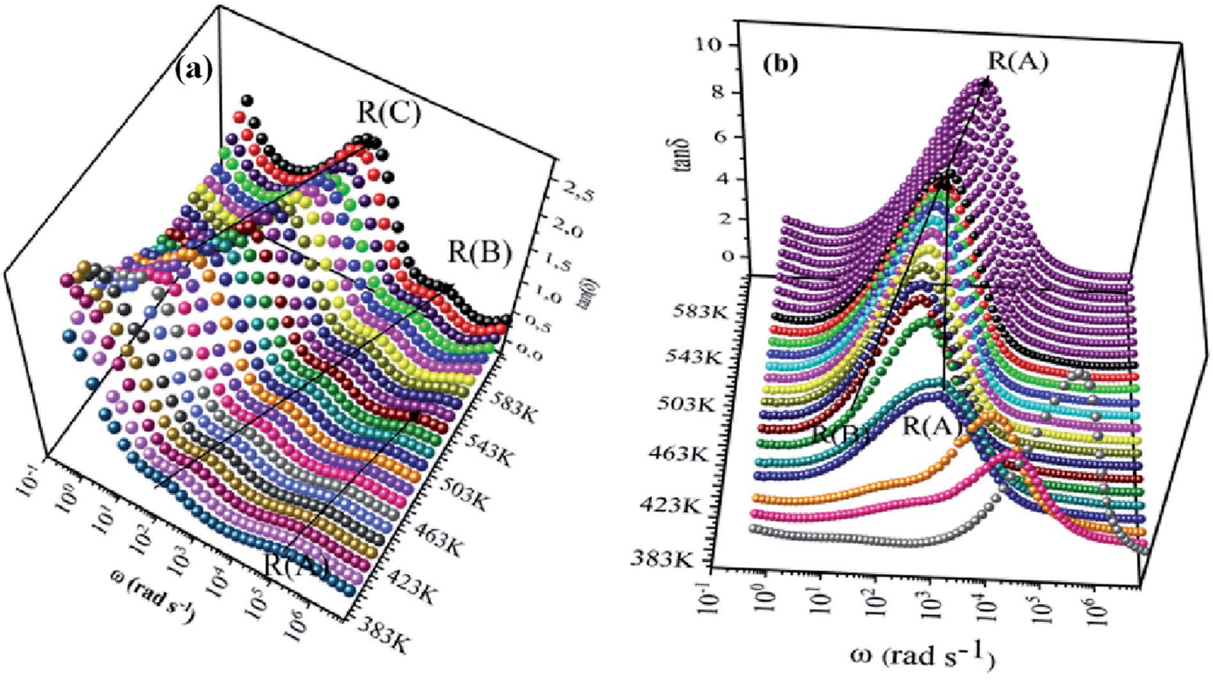

Fig. 6 Frequency dependence of tan $\delta$ at various temperatures for NCS-SS (a) and NCS-CP (b) as a function of temperature.

with decreasing frequency, we could attribute this dielectric dispersion phenomenon to a thermally-activated process. The relaxation time for the medium and high frequency relaxations was very close. For NCS-CP, two clear peaks are observed in the frequency dependence of the dielectric loss as shown in Fig. 6(b). The first one occurred at mid frequency range 500–3700 Hz (relaxation B) and the second was presented at high frequency range $8 \times 10^3$–$5 \times 10^5$ Hz (relaxation A). The relaxation peaks moved toward high frequencies with the increase in the temperature, indicating that the relaxation processes in both NCS samples are temperature dependent. In the main processes, the Na and O positions were quite dynamic, while the Co–Si network remained relatively undisturbed to maintain the stability of the structure as a function of temperature. Accordingly, understanding the distinction of the relaxation process between NCS-SS and NCS-CP provides a more comprehensive image of the system dynamics and the transport mechanisms. First, NCS-SS (with the *Pna*2$_1$ space group) had lower local Na coordination symmetry than NCS-CP (with the *Pbca* space group) which was caused by the different silicon and cobalt sources.[29,30] Second, the NCS-SS material presented two different charge carriers Na(1) and Na(2) in two equivalent cavities. However, NCS-CP presented four charge carriers Na(1), Na(2), Na(3) and Na(4) in two non-equivalent cavities.[31] The Na$^+$ environment in NCS-CP was more congested than NCS-SS, because of the duplication of Si and Co and the presence of Cl$^-$.

We notice that the Coulombic attraction and the network are based on the increase in Na$^+$, but the effect of the cation–cation repulsion and the steric effects can facilitate the jump of the Na$^+$-ions along the canals. In this context, the above-listed results also imply that the Na-ions are less tight in NCS-CP than in NCS-SS, especially that the volume of NCS-SS (405.30 Å$^3$) is lower than NCS-CP (771.74 Å$^3$). Therefore, the connection of Na polyhedra leads to a flat energy landscape for sodium cations, which is beneficial for ion transport. As these sites are supposed to be metastable for the migration of sodium-ions, the migration energy barriers of sodium-ions depend on the crystallographic sites. In fact, the higher Na–O average bond distances (2.2587 Å) in NCS-SS with respect to in the NCS-CP ones (2.2632 Å) induces a decreasing of the attraction force between Na$^+$ and O$^{2-}$ and the ions becomes less attached to the crystal.

### 3.5. Activation energy

To bring out the relaxation response in the prepared materials, it is necessary to find the activation energy of the relaxation process for each composition. Fig. 7(a) and (b) are plotted the variation of ln($\omega_{\max}$) as a function of the reciprocal of the temperature. A thermally-activated relaxation process is observed in both samples and confirms the semiconducting characteristic of samples. Notably, a humidity effect appears at around $T = 533$ K for NCS-CP sample.

The $\omega_{\max}$ data were fitted using the Arrhenius law equation:[32]

$$\omega_{\max} = \omega_0 \exp\left(-\frac{E_a}{k_B T}\right) \tag{2}$$

where $E_a$ is the activation energy required for the thermally-activated process, $\omega_0$ represents the pre-exponential factor and $k_B$ is the Boltzmann constant. The activation energy is presented in Table 5. It is notable that the activation energies of NCS-SS were higher than those of NCS-CP. The experimental data exhibits a deviation from the Arrhenius law in several materials, which shows the polaron relaxation related to localized charge carriers.[33–37]

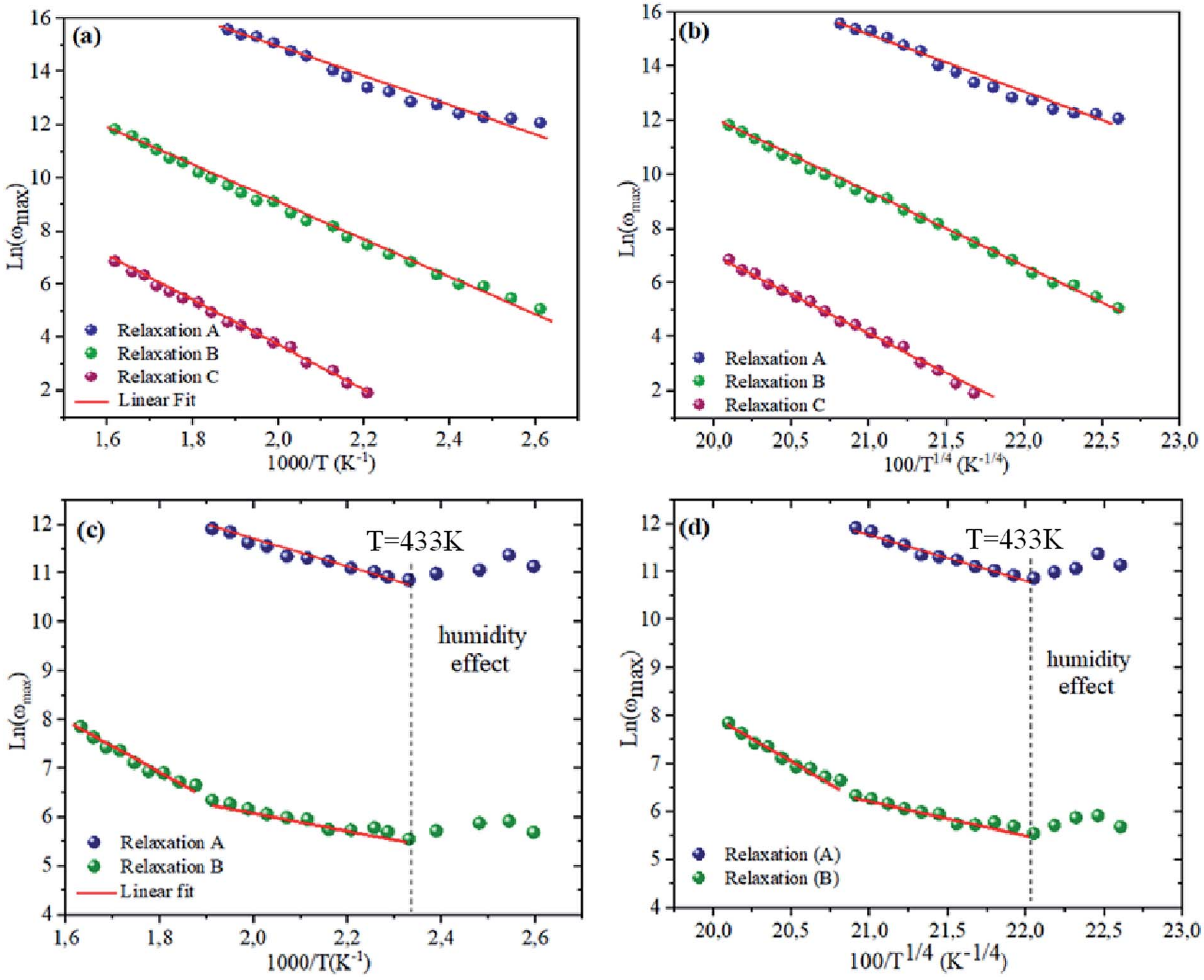

Fig. 7 (a and c) dependence of relaxation frequency $\omega$ on temperature with $\ln(\omega_{\max})$ *vs.* $1000/T$. The solid lines are the best-fitting results according to eqn (2). (b and d) The dependence of the relaxation frequency $\omega$ on temperature with $\ln(\omega_{\max})$ *vs.* $100/T^{1/4}$. The solid lines are the best-fitting results according to eqn (3).

Table 5 Activation energy obtained from the curves in Fig. 7(a) and (c)

| Relaxation | NCS-SS | NCS-CP |
|---|---|---|
| Relaxation A | 0.45 eV | 0.25 eV |
| Relaxation B | 0.59 eV | 0.41 eV (at high temperature)<br>0.18 eV (at low temperature) |
| Relaxation C | 0.71 eV | |

Moreover, a Mott's variable-range-hopping mechanism for polarons could fit better as described by eqn (3).[38]

$$\omega = \omega_1 \exp\left[-\left(\frac{T_1}{T}\right)^{1/4}\right] \tag{3}$$

where $\omega_1$ and $T_1$ are two fitting constants. The solid lines of this model are shown in the inset of Fig. 7(c) and (d). The values $T_1$ for NCS-SS were $2.18 \times 10^7$ K, $5.12 \times 10^7$ K and $8.31 \times 10^7$ K for relaxations (A), (B) and (C) respectively. The values for NCS-CP were determined to be $1.8 \times 10^7$ K for relaxation (A) and $7.59 \times 10^7$ K between 533 K and 613 K as well as $8.4 \times 10^7$ K below 533 K for relaxation (B). The $T^{-1/4}$ law confirmed the polaron relaxation in NCS samples.[11,39] The quasiparticle (polaron) could move between different vacant sites.

The transition energy of a polaron can be expressed by the following equation:[11]

$$W = 0.25k_B(T_1)^{\frac{1}{4}}T^{\frac{3}{4}} \tag{4}$$

The hopping energy $W$ calculated by eqn (4) increased from 0.15 eV at 383 K to 0.19 eV at 533 K for the relaxation (A), from 0.15 eV at 383 K to 0.22 eV at 613 K for the relaxation (B) and from 0.2 eV at 453 K to 0.25 eV at 613 K for NCS-SS. The sample NCS-CP exhibited the same behavior. The W values were found to be 0.21–0.26 eV below 513 K and 0.21–0.24 eV at high temperature for the relaxation (A) and 0.79–0.89 eV for the relaxation (B). The activation energy for the relaxation indicates that the relaxation mechanism for the two NCS materials is associated with polaron hopping based on charge carriers in order to account for the origin of a dielectric relaxation observed in NCS-SS and NCS-CP. These results hint that the sodium-ions

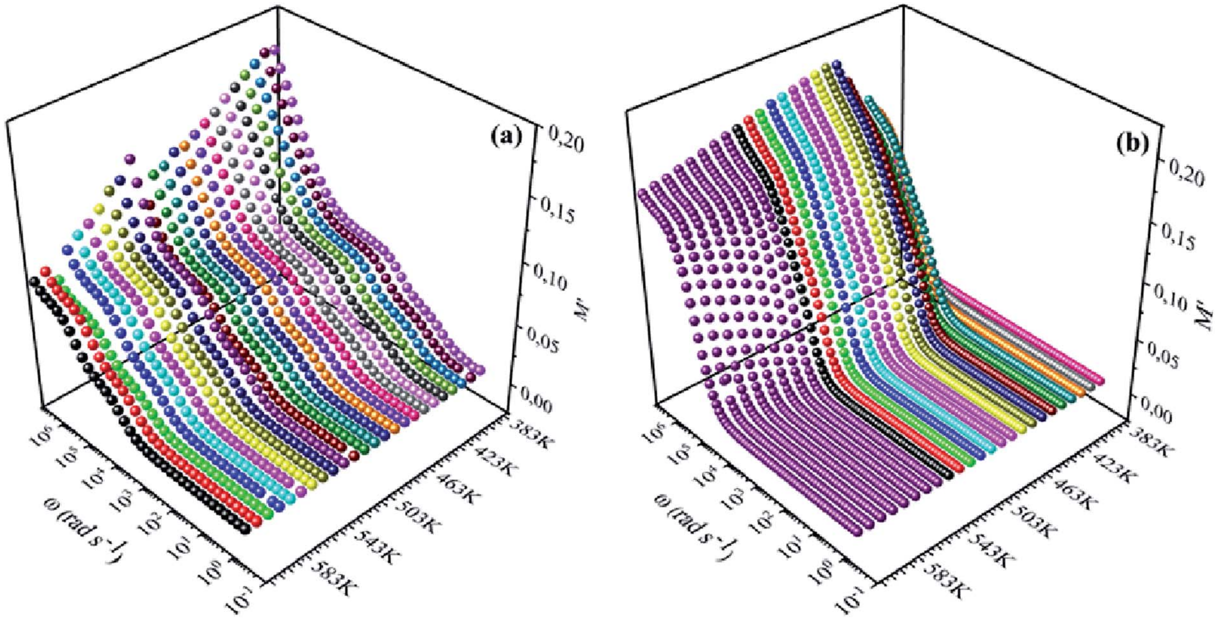

Fig. 8 Frequency dependence of real of electric modulus ($M'$) for (a) NCS-SS and (b) NCS-CP at various temperatures.

over these sites probably pass from Na(4*a*) for NCS-SS and Na(8*c*) for NCS-CP to other sites.

### 3.6. Frequency and temperature dependence of the electric modulus formalisms

To emphasize the relaxation phenomena, a study of the complex modulus at various temperatures was carried out in the same frequency range. The electric modulus was employed to investigate the polaron relaxation and to avoid the dynamical aspects of the electrical transport phenomena in the NCS samples.[40] The complex electric modulus ($M^*$) could be calculated by the conversion formula (eqn (5)) using the complex dielectric constant ($\varepsilon^*$), which is defined by:

$$M^* = \frac{1}{\varepsilon^*} = \frac{\varepsilon'}{\varepsilon'^2 + \varepsilon''^2} + \frac{i\varepsilon''}{\varepsilon'^2 + \varepsilon''^2} = M' + iM'' \tag{5}$$

where $M' = \dfrac{\varepsilon'}{\varepsilon'^2 + \varepsilon''^2}$ is the real part of complex modulus and $M'' = \dfrac{\varepsilon''}{\varepsilon'^2 + \varepsilon''^2}$ is the imaginary part of the complex modulus.

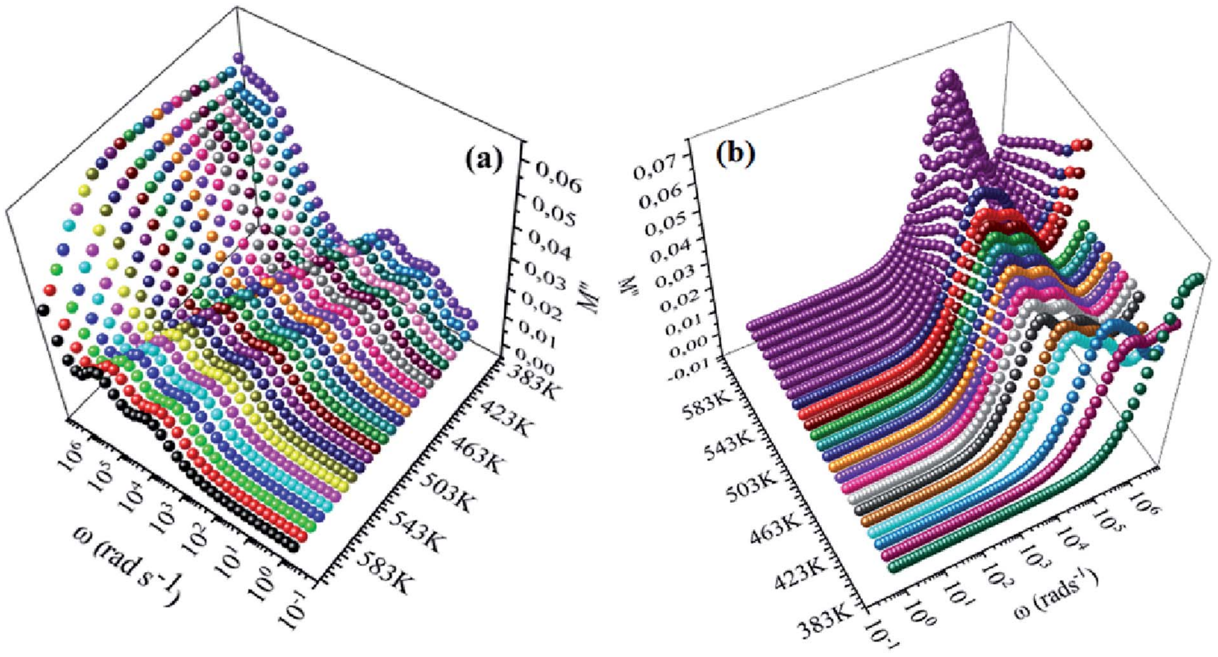

Fig. 9 Frequency dependence of imaginary of electric modulus ($M''$) for NCS-SS (a) and NCS-CP (b) at various temperatures.

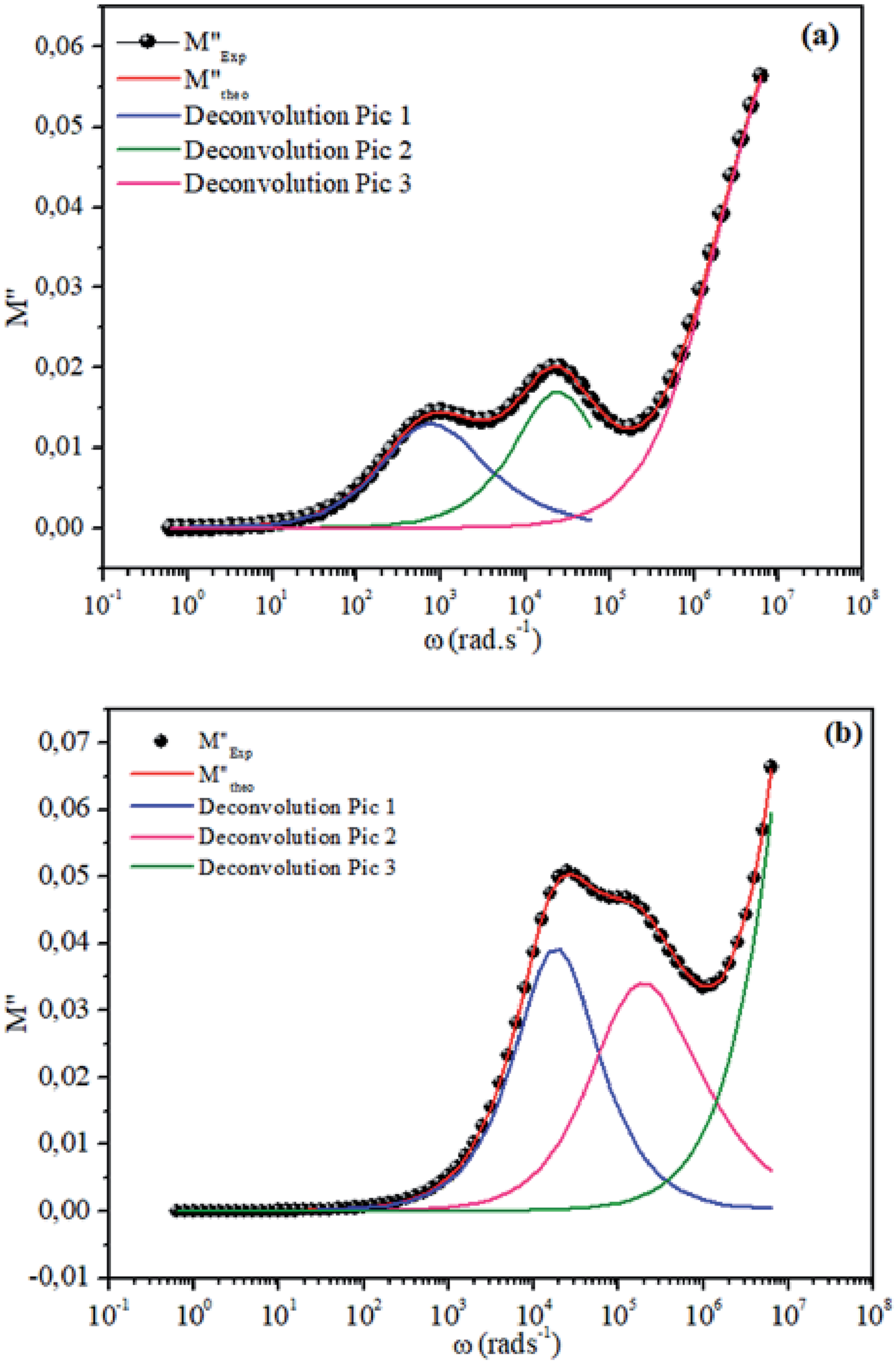

Fig. 10 Deconvolution of experimental imaginary parts of impedance ($M''$) as a function of angular frequency for NCS-SS (a) and NCS-CP (b) at 513 K used eqn (6).

Fig. 8(a), (b), 9(a) and (b) show the variation of the real and imaginary parts of the modulus as a function of angular frequency at various temperatures for NCS-SS and NCS-CP. At low frequencies, $M'$ exhibited very small values and tended to zero and, thus, suggesting the suppression of the electrode polarization effect.[41] As the frequency increased, $M'$ climbed to a maximum asymptotic value defined as $M''_{\infty}$ due to the distribution of relaxation processes over a range of frequencies. Both samples produced a two-step decrease in $M'$ in the measured temperature range, while the NCS-CP peaks shifted to one step above 533 K. Correspondingly, $M''$ showed two peaks in the same temperature range. The modulus spectra presented different relaxation mechanisms which depend upon temperature and frequency regions. We observe that NCS-SS appearing in $M''$ along the temperature ranges. NCS-CP revealed two peaks, which shifted to a single peak at high temperature. To distinguish localized dielectric relaxation processes, R. Gerhardt proposed two ways: as far as NCS-CP is concerned, this material presented a pure conduction process (relaxation B), which could be seen as a relaxation peak observed in the frequency spectra of the imaginary component $M''$ and no clear peak appeared in the corresponding plot of $\varepsilon'$ and $\varepsilon''$, while for relaxation A, this sample (NCS-CP) showed weak peaks of $\varepsilon'$ and $\varepsilon''$. This mixed process was related to the presence of two charges carriers ($Na^+$). As regards NCS-SS, this material indicated a dielectric relaxation process as the relaxation peaks appeared in all the representations of $M''$, tan $\delta$, $\varepsilon'$ and $\varepsilon''$.[42,43] The peaks at low and high temperatures might be attributed to the existence of dissociate Na-ions or steady species caused by linked Na in NCS samples. Whilst, the peak overlap (above 533 K) is attributed either to cavity deformation or the two charge carriers $Na^+$ are the same response at high temperatures in NCS-CP.[44,45] The spectra of $M''$ peaks at both high and mid frequencies suggest that two processes contribute to the

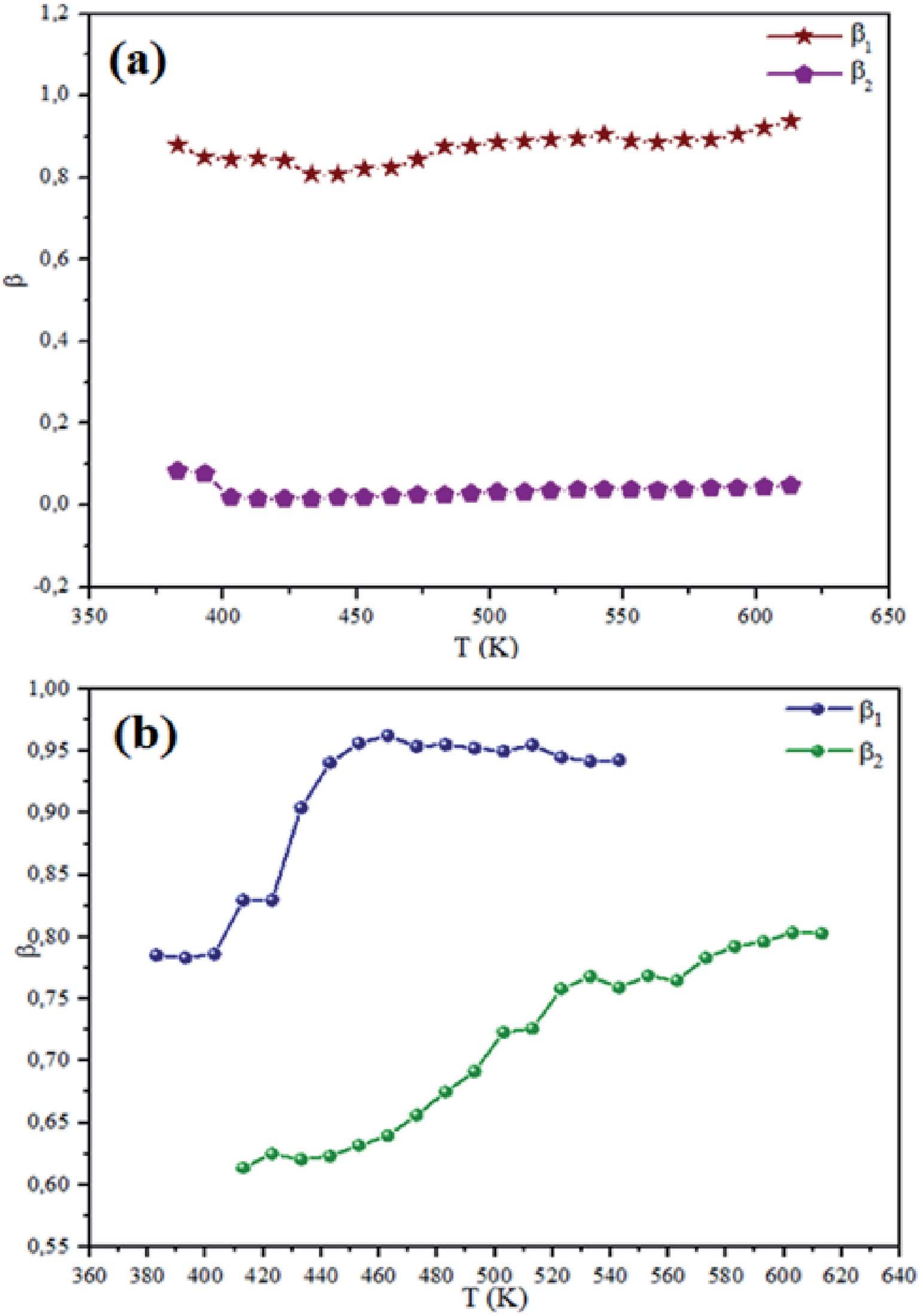

Fig. 11 Temperature dependence of the NCS-SS (a) and NCS-CP (b) at various temperatures.

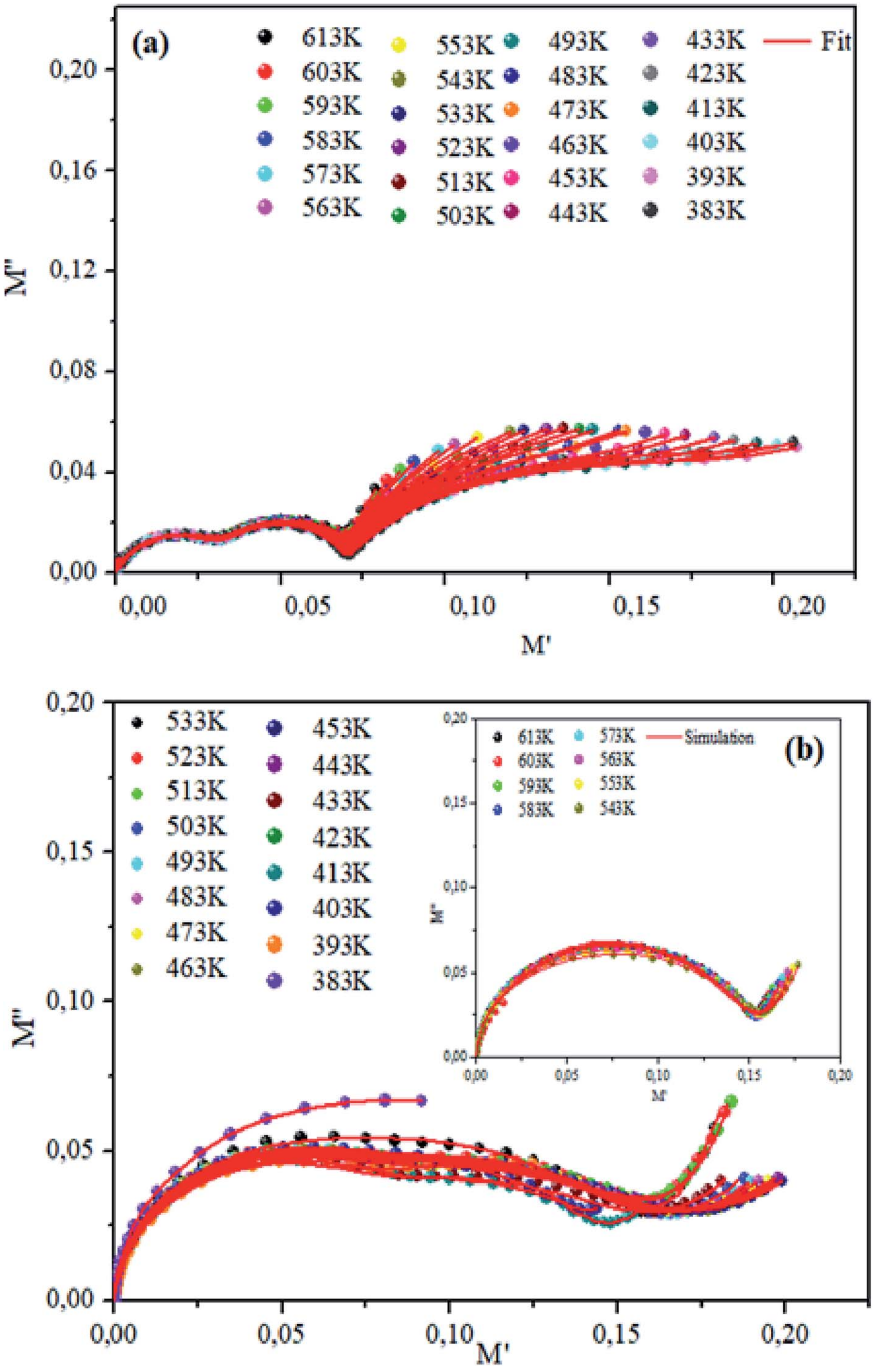

Fig. 12 Plots of imaginary modulus $M''$ *vs.* $M'$ real modulus for NCS-SS (a) and NCS-CP (b) at various temperatures.

diffusion of two Na charge carriers. One of these processes relaxed at the high frequency region but the contribution of the other process appeared as a peak in the mid frequency region. The values of $M''_{\max}$ shifted to the high frequency values with the increase in the temperature. The imaginary part of the electric modulus in different temperatures has been fitted with the function proposed by Bergman:[46]

$$M'' = \sum_{i=1}^{3} \frac{M''_{i\,\max}}{\left[(1-\beta_i)+\left(\frac{\beta_i}{1+\beta_i}\right)\right]\left[\left(\frac{\omega_{i\,\max}}{\omega}\right)+\left(\frac{\omega}{\omega_{i\,\max}}\right)\beta_i\right]} \tag{6}$$

where the $M''_{\max}$ is the maximum peak value of $M''$, $\omega_{\max}$ is the corresponding frequency and the index $\beta$ indicates the degree of deviation from the Debye-type relaxation.

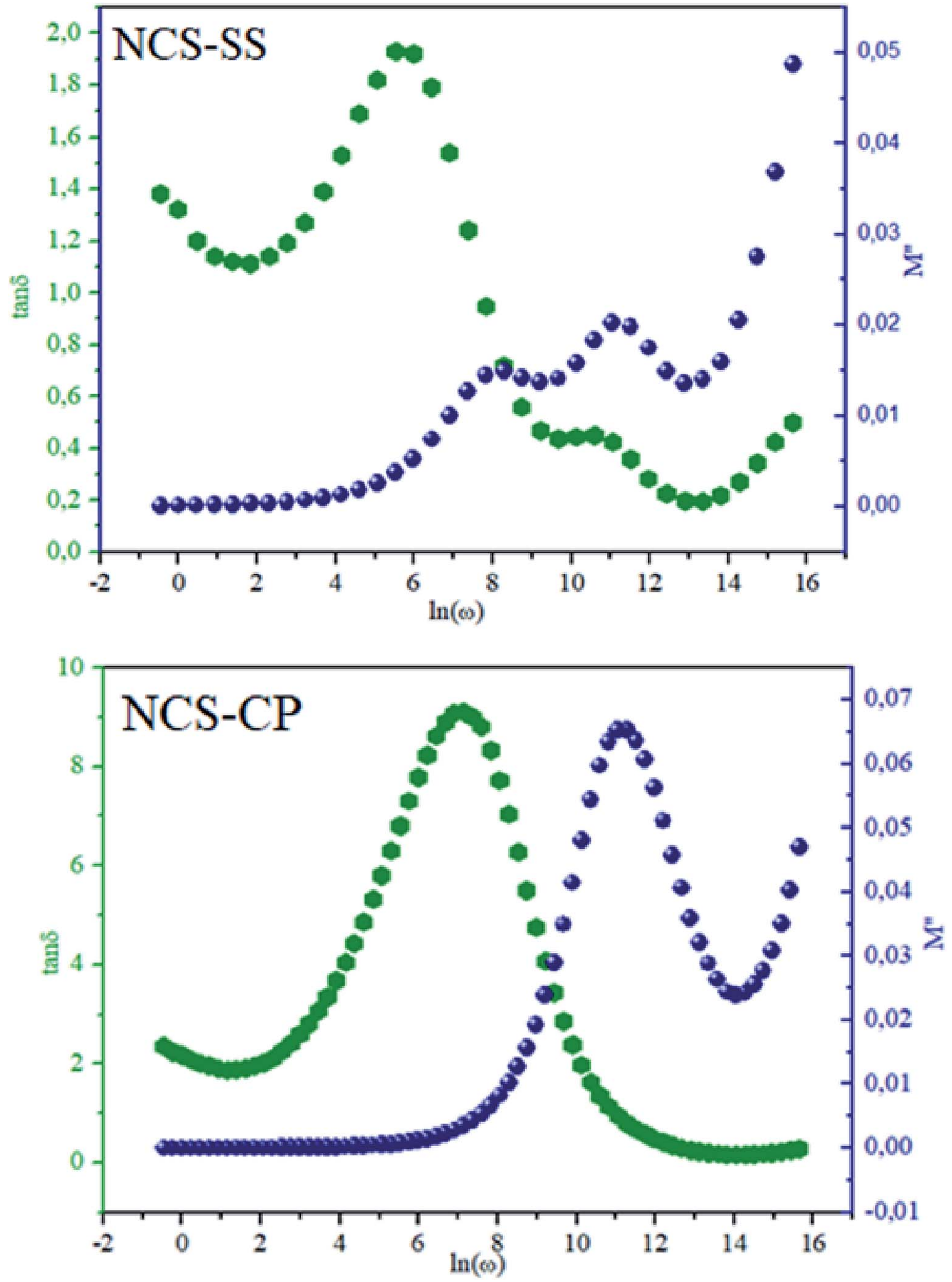

Fig. 13 Frequency dependence of relaxation peaks, $M''$ and tan $\delta$ for the two NSC compounds at 573 K.

The theoretical fit and peak deconvolution (eqn (6)) of the experimental data are shown by solid lines in Fig. 10(a) and (b). It can be seen that the model fits the experimental data very well. The fit values of $\beta$ ($\beta < 1$) suggest a non-Debye-type dielectric relaxation.[47] Fig. 11 shows the dependence of $\beta$ values on the variety of temperatures. For NCS-SS, $\beta$ varied slightly in the temperature range which indicates stability of the number of Na-ions available for short distance conduction. This result suggests that the polarons are stable in the dielectric process with the increase in the temperature. NCS-CP demonstrated higher values of $\beta_2$ when the value of $\beta_1$ increased to 0.96 below 453 K, and then slightly decreased to 0.92 as soon as the temperature went up to 613 K. The increase in $\beta$ implies that there is a decrease in the number of sodium-ions available for short distance conduction where $Na^+$-ions have a higher probability of being attracted by $Cl^-$-ions.[48,49] The complex electrical modulus of the NCS-SS sample (Fig. 12(a)) displays three semicircles. At low and mid frequencies, the arcs were perfectly overlapped into a single master curve, indicating that the underlying conduction mechanism remains the same, while at high frequency, we can seem a dispersion phenomena. As a result, the different contributions are linked to the transport

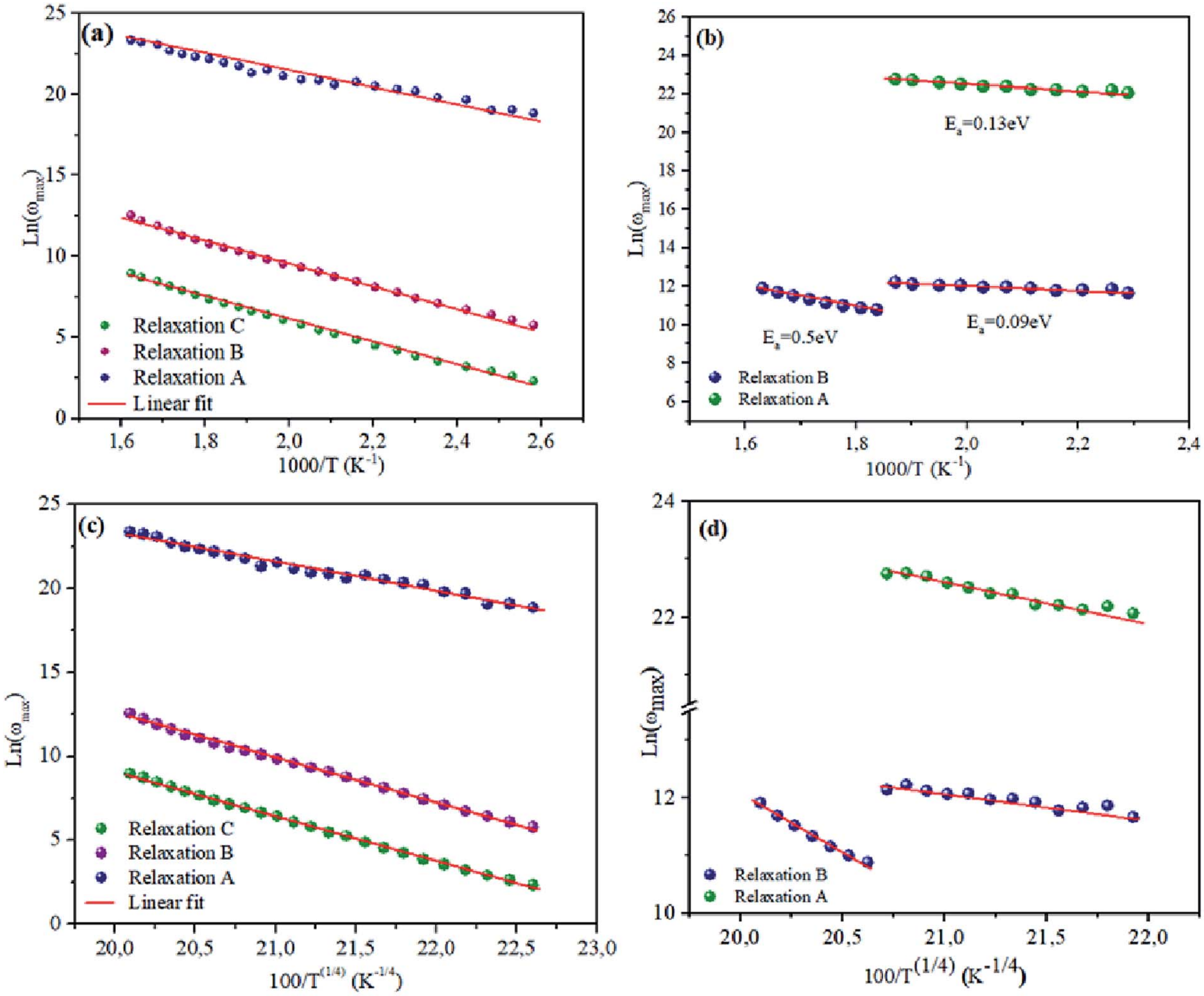

Fig. 14 Dependence of relaxation frequency $\omega$ on temperature with ln $\omega_{\max}$ *vs.* 1000/$T$ (a and b) and ln $\omega_{\max}$ *vs.* 100/$T$(1/4) (c and d) for NCS-SS and NCS-CP, respectively.

mechanism of $Na^+$ in or between cavities $T_1$ and $T_2$. On the other hand, NCS-CP displays only one semicircle between 543 K and 613 K, while it shows two discarded semicircles below 533 K (Fig. 12(b)). This result confirms that cavity is deformed at high temperature. The increase of temperature facilitates the long-range hopping movement of charge carriers $Na^+$. This result is confirmed by the representations of $M''$ and tan $\delta$ as a function of the logarithmic frequency measured at 573 K. We can see in Fig. 13 that the peak positions of $M''$ and tan $\delta$ were more similar for NCS-SS than for NCS-CP. Therefore, we distinguish that, the peak positions between $M''$ and tan $\delta$ were overlapped for NCS-SS. This indicates that long range and localized relaxations occur simultaneously. However, for NCS-CP, the two peak positions were dissimilar indicating a delocalized or a long-range transport mechanism.[50] The dielectric relaxations processes suggest that the diffusion pathway of two sodium-ions could migrate over the same trajectories.[11] The shift of the relaxation peak corresponds to the relaxation process towards higher frequencies with an increase in temperature which brings out a thermally-activated dielectric relaxation.[51] At any temperature, the frequency $\omega_{\max}$ defines the relaxation time $\tau\omega = 1$. In order to obtain the required activation energy for the dielectric relaxation process, the corresponding graphs of $M''$as a function of $\omega$ and $T$ for various values of $\omega_{\max}$ are shown in Fig. 14. The temperature dependence of the characteristic relaxation frequency satisfies the Arrhenius law given by;[32]

$$\omega_{\max} = \omega_0 \exp\left(-\frac{E_a}{k_B T}\right) \tag{7}$$

Consequently, it should be noted that $E_a$ values which were obtained for the analysis of the results plotted in Fig. 14 were higher for NCS-SS than for NCS-CP. For the relaxation R(A), the calculated activation energies were 0.6 eV and 0.13 eV for NCS-SS and NCS-CP respectively. The $E_a$ values for the relaxation R(B) were found to be 0.6, 0.59 eV and 0.5–0.09 eV for NCS-SS and NCS-CP respectively. The relaxation R(C) yielded 0.39 eV for NCS-SS. The variations of ($\omega_{\max}$) obey the same Arrhenius law of eqn (3) (Fig. 14(c) and (d)). The parameter $T_1$ was calculated to be $4.7 \times 10^7$ K, $5.15 \times 10^7$ K and $8.98 \times 10^7$ K for R(A), R(B), R(C) respectively in NCS-SS. These values were equal to the ones obtained by the dielectric loss. The similar behavior of the relaxation process between the modulus and tan $\delta$ indicates that they originated from the same mechanism. However, NCS-CP pointed to very different values from those obtained by tan $\delta$. The parameter $T_1$ was calculated to be $0.16 \times 10^7$ K for R(A) and $1.51 \times 10^7$ K and $0.29 \times 10^7$ K for R(B).

Generally, it is suggested that the dielectric relaxation might be due to such intrinsic contributions as the two types of charge carriers (sodium ions). In (Section 3.3), we pointed to the existence of the $Cl^-$-ion in NCS-CP. In fact, $Cl^-$ was located at the neighboring sites of Na and it had a different valence stability compared with $O^{2-}$. Therefore, the only conclusion which could be drawn is that the Na site may be fully-occupied.[52] Besides, the cationic distribution results from the energy minimization between: (1st) the electrostatic repulsions that tend to separate $Na^+$-ions in the ($a$, $c$) plan, (2nd) the $Na^+$–$Co^{2+}$ repulsion through the common face between the $NaO_4$ and $CoO_4$ polyhedra, and (3rd) the electron–electron interaction in the cobalt layer. As all these parameters were very sensitive to the sodium content, various cationic distributions were observed all along the compositions.[53] This brought the $Na^+$-ions closer to the $Co^{2+}$-ions and consequently generated a repulsive force between the two cations. Yet, the presence of $Cl^-$ surface at the level of the compound NCS-CP could induce other electrostatic attractions which lead to lower activation energy and higher diffusion mechanism on the neighboring sites close to the Na migration route.[54] We suppose, in consequence, that the dielectric relaxation is associated with the cavity.

## 4. Conclusions

$Na_2CoSiO_4$ samples have been successfully synthesized by the improved solid-state and co-precipitation methods. The NCS samples were found to crystallize in the orthorhombic symmetry with the $Pna2_1$ and $Pbca$ space groups for NCS-SS and NCS-CP respectively. The SEM images showed the appearance of particles of different sizes and forms due to the chemical process and sintered temperatures. The frequency-dependent plots of $M''$, $\varepsilon'$, $\varepsilon''$ and tan $\delta$ at different temperatures showed that there were two different relaxation regions in NCS-CP and three relaxations in NCS-SS. The low-frequency region was associated with the space charge, while the high-frequency region was associated with the confined charge carriers that moved over two different cavities. Furthermore, the dielectric proprieties of $Na_2CoSiO_4$ which were associated with the migration of the sodium-ions have been studied at various temperatures and frequencies. Consequently, we found a dielectric relaxation process for NCS-SS and a mixture of dielectric relaxation and conduction processes for NCS-CP. Interestingly, the transition energy was associated with a transition of the polaron between localized states with phonon assistance for NCS-SS and a transition of the polaron between delocalized states with phonon assistance for NCS-CP. The polaron relaxation process with the $T^{-1/4}$ behavior at different temperatures is attributed to the charge carriers that can move between mixed valences of ions. The activation energy of NCS-SS was higher than that of NCS-CP. The different values of activation energies deduced from different formalisms suggest that the same charge species were responsible for the relaxation of NCS-SS; however, for NCS-CP, the different values of activation energies were caused by the presence of surfaced $Cl^-$ and cavity ($T_2$) depending on temperature. We also found that for this sample, a diffusion process at high temperature was associated to the displacement of Na-ions to the cavity equivalent to $T_1$. This gives an insight into the diffusion behavior of Na-ions at different chemical environments and proves the previously-mentioned results to build the relationship between the migration of sodium-ions and the dielectric relaxation for sodium-based electrode materials.

## Conflicts of interest

There are no conflicts to declare.

## References

1 A. Nyten, A. Abouimrane, M. Armand, T. Gustafsson and J. O. Thomas, Electrochemical performance of $Li_2FeSiO_4$ as a new Li-battery cathode material, *Electrochem. Commun.*, 2005, **7**, 156–160.

2 R. Dominko, M. Bele, M. Gaberscek, A. Meden, M. Remskar and J. Jamnik, Structure and electrochemical performance of $Li_2MnSiO_4$ and $Li_2FeSiO_4$ as potential Li-battery cathode materials, *Electrochem. Commun.*, 2006, **8**, 217–222.

3 Z. L. Gong, Y. X. Li and Y. Yang, Synthesis and characterization of $Li_2Mn_xFe_{1-x}SiO_4$ as a cathode material for lithium-ion batteries, *Electrochem. Solid-State Lett.*, 2006, **9**, A542–A544.

4 M. M. Thackeray, P. J. Johnson, L. A. De Picciotto, P. G. Bruce and J. B. Goodenough, Electrochemical extraction of lithium from $LiMn_2O_4$, *Mater. Res. Bull.*, 1984, **19**, 179.

5 L. Wang, M. Wang and D. Zhao, Thermoelectric properties of c-axis oriented Ni-substituted $NaCoO_2$ thermoelectric oxide by the citric acid complex method, *J. Alloys Compd.*, 2009, **471**, 519–523.

6 B. L. Ellis, W. R. M. Makahnouk, Y. Makimura, K. Toghill and L. F. Nazar, A multifunctional 3.5 V iron-based phosphate cathode for rechargeable batteries, *Nat. Mater.*, 2007, **6**, 749–753.

7 H. Bordeneuve, D. J. Walesb, J. W. Andrew, H. V. Doan, V. P. Ting and C. R. Bowena, Understanding the AC conductivity and permittivity of trapdoor chabazites for future development of next-generation gas sensors, *Microporous Mesoporous Mater.*, 2018, **260**, 208–216.

8 P. Fisher, M. Luján, F. Kubel and H. Schmid, Crystal structure and magnetic ordering in magnetoelectric $KNiPO_4$ investigated by means of X-ray and neutron diffraction, *Ferroelectrics*, 1994, **162**, 37–44.

9 A. Panigrahi, S. Nishimura, T. Shimada, E. Watanabe, W. Zhao, G. Oyama and A. Yamada, Sodium iron (II) pyrosilicate $Na_2Fe_2Si_2O_7$: a potential cathode material in the $Na_2O$-FeO-$SiO_2$ system, *Chem. Mater.*, 2017, **29**, 4361–4366.

10 W. Shun-qing, Z. Zi-zhong, Y. Yong and H. Zhu-feng, Effects of Na-substitution on structural and electronic properties of $Li_2CoSiO_4$ cathode material, *Trans. Nonferrous Met. Soc.*, 2009, **19**, 182–186.

11 S. Ren, J. Liu, D. Wang, J. Zhang, X. Ma, M. Knapp, L. Liu and H. Ehrenberg, Dielectric relaxation behavior induced by lithium migration in $Li_4Ti_5O_{12}$ spinel, *J. Alloys Compd.*, 2019, **793**, 678–685.

12 R. Vaish and K. B. R Varma, The glass transition and crystallization kinetic studies on $BaNaB_9O_{15}$ glasses, *J. Phys. D: Appl. Phys.*, 2008, **41**, 165401.

13 P. G. Bruce, B. Scrosati and J. M. Tarascon, Nanomaterials for rechargeable lithium batteries, *Angew. Chem., Int. Ed.*, 2008, **47**, 29–30.

14 T. X. T. Sayle, R. R. Maphanga, P. E. Ngoepe and D. C. Sayle, Predicting the Electrochemical Properties of $MnO_2$ Nanomaterials Used in Rechargeable Li Batteries: Simulating Nanostructure at the Atomistic Level, *J. Am. Chem. Soc.*, 2009, **131**, 6161.

15 J. C. Treacher, S. M. Wood, M. S. Islam and E. Kendrick, $Na_2CoSiO_4$ as a cathode material for sodium-ion batteries: structure, electrochemistry and diffusion pathways, *Phys. Chem. Chem. Phys.*, 2016, **18**(48), 32744–32752.

16 Y. Li, W. Sun, d J. Liang, H. Sun, I. Di Marco, L. Ni, S. Tang and J. Zhang, Understanding the electrochemical properties of A 2 MSiO 4 (A= Li and Na; M= Fe, Mn, Co and Ni) and the Na doping effect on $Li_2MSiO_4$ from first-principles, *J. Mater. Chem. A*, 2016, **4**, 17455–17463.

17 X. Zhao, S. Q. Wu, X. Lv, M. C. Nguyen, C.-Z. Wang, Z. Lin, Z. Z. Zhu and K.-M. Ho, Exploration of tetrahedral structures in silicate cathodes using a motif-network scheme, *Sci. Rep.*, 2015, **5**, 15555.

18 H. M. Rietveld, A profile refinement method for nuclear and magnetic structures, *J. Appl. Crystallogr.*, 1969, **2**, 65–71.

19 L. Zhu, Y.-R. Zeng, J. Wen, L. Li and T.-M. Cheng, Structural and electrochemical properties of $Na_2FeSiO_4$ polymorphs for sodium-ion batteries, *Electrochim. Acta*, 2018, **292**, 190–198.

20 V. Kahlenberg, G. DoK rsam, M. Wendschuh-Josties and R. X. Fischer, The Crystal Structure of δ-$Na_2Si_2O_5$, *J. Solid State Chem.*, 1999, **146**, 380–386.

21 P. Wu, S. Q. Wu, X. Lv, X. Zhao, Z. Ye, Z. Lin, C. Z. Wang and K. M. Ho, Fe–Si networks in $Na_2FeSiO_4$ cathode materials, *Phys. Chem. Chem. Phys.*, 2016, **18**, 23916–23922.

22 S. Frostsing, J. Grins, D. Lougr and P.-E. Werner, Synthesis, structure and conductivity of $Ag_2ZnSiO_4$, $Ag_2ZnGeO_4$ and $Ag_2BeSiO_4$, *Solid State Ionics*, 1988, **32**, 131.

23 B. Maksimov, R. Tamazyan, M. I. Sirota, S. Frosting, J. Grins and M. Nygren, The crystal structure and twinning laws of the orthorhombic modification of $Na_2BeSiO_4$, *J. Solid State Chem.*, 1990, **86**, 64.

24 I. Belharouak, A. Abouimrane and K. Amine, Structural and electrochemical characterization of $Li_2MnSiO_4$ cathode material, *J. Phys. Chem. C*, 2009, **113**(48), 20733–20737.

25 S. P. Guo, J. C. Li, Q. T. Xu, Z. Ma and H. G. Xue, Recent achievements on polyanion-type compounds for sodium-ion batteries: syntheses, crystal chemistry and electrochemical performance, *J. Power Sources*, 2017, **361**, 285–299.

26 B. Senthilkumar, K. Vijaya Sankar, L. Vasylechko, L. Yun-Sung and R. Kalai Selvan, Synthesis and electrochemical performances of maricite-$NaMPO_4$ (M= Ni, Co, Mn) electrodes for hybrid supercapacitors, *RSC Adv.*, 2014, **4**, 53192–53200.

27 H. Yoshida, N. Yabuuchi and S. Komaba, $NaFe_{0.5}Co_{0.5}O_2$ as High Energy and Power Positive Electrode for Na-Ion Batteries, *Electrochem. Commun.*, 2013, **34**, 60–63.

28 S. Frostang, J. Grins and M. Nygren, Ionic Conductivity Studies and Phase Analysis of the $Na_2BeSiO_4$-$Na_2BeSi_2O_6$ System, *J. Solid State Chem.*, 1988, **72**, 92–99.

29 J. Grins and D. Louijr, A rietveld refinement of the structure of $K_2ZnGeO_4$ and its relationship to a revised model of the $KGaO_2$ structure type, *Solid State Chem.*, 1990, **87**, 114–123.

30 S. Harm, A.-K. Hatz, C. Schneider, C. Hoefer, C. Hoch and V. Bettina, Lotsch, Finding the Right Blend: Interplay Between Structure and Sodium Ion Conductivity in the System $Na_5AlS_4$–$Na_4SiS_4$, *Front. Chem.*, 2020, **8**, 90.

31 W. Baur, T. Ohta and R. Shannon, Structure of Magnesium Disodium Silicate $Na_2MgSiO_4$ and Ionic Conductivity in Tetrahedral Structures, *Acta Crystallogr., Sect. B: Struct. Crystallogr. Cryst. Chem.*, 1981, **37**, 1483–1491.

32 L. Liu, M. Wu, Y. Huang, Z. Yang, L. Fang and C. Hu, Frequency and temperature dependent dielectric and conductivity behavior of $0.95(K_{0.5}Na_{0.5})$ $NbO_3$-$0.05BaTiO_3$ ceramic, *Mater. Chem. Phys.*, 2011, **126**, 769–772.

33 I. M. Hodge, M. D. Ingram and A. R. West, Impedance and modulus spectroscopy of polycrystalline solid electrolytes, *J. Electroanal. Chem.*, 1976, **74**, 125–143.

34 R. Gerhardt, Impedance and dielectric spectroscopy revisited: distinguishing localized relaxation from long-range conductivity, *J. Phys. Chem. Solids*, 1994, **55**, 1491–1506.

35 S. K. Deshpande, S. N. Achary, R. Mani, J. Gopalakrishnan and A. K. Tyagi, Low-temperature polaronic relaxations with variable range hopping conductivity in $FeTiMO_6$ (M = Ta, Nb, Sb), *Phys. Rev. B: Condens. Matter Mater. Phys.*, 2011, **84**, 064301.

36 M. Younas, M. Nadeem, M. Idrees and M. J. Akhtar, Jahn-Teller assisted polaronic hole hopping as a charge transport mechanism in CuO nanograins, *Appl. Phys. Lett.*, 2012, **100**, 152103.

37 A. Leonarska, M. Kądziołka-Gaweł, A. Z. Szeremeta, R. Bujakiewicz-Korońska, A. Kalvane and A. Molak, Electric relaxation and $Mn^{3+}/Mn^{4+}$ charge transfer in Fe doped $Bi_{12}MnO_{20}$–$BiMn_2O_5$ structural self-composite, *J. Mater. Sci.*, 2017, **52**, 2222–2231.

38 N. F. Mott, Conduction in non-crystalline materials, *Philos. Mag.*, 1987, **19**, 835–852.

39 J. Liua, Q. Liub, Z. Nieb, S. Nieb, D. Lub and P. Zhua, Dielectric relaxations in fine-grained $SrTiO_3$ ceramics with Cu and Nb co-doping, *Ceram. Int.*, 2019, **45**, 10334–10341.

40 P. B. Macedo, C. T. Moynihan and R. Bose, The longtime aspects of this correlation function, which are obtainable

by bridge techniques at temperatures approaching the glass transition, *Phys. Chem. Glasses*, 1972, **13**, 171–176.

41 R. M. Mahani and S. Y. Marzouk, *J. Alloys Compd.*, 2013, **579**, 394–400.

42 L. Zhang and Z.-J. Tang, Polaron relaxation and variable-range-hopping conductivity in the giant-dielectric-constant material $CaCu_3Ti_4O_{12}$, *Phys. Rev. B: Condens. Matter Mater. Phys.*, 2004, **70**, 174306.

43 C. C. Wang and L. W. Zhang, Polaron relaxation related to localized charge carriers in $CaCu_3Ti_4O_{12}$, *Appl. Phys. Lett.*, 2007, **90**, 142905.

44 K. K. Lily, K. Prasad and R. N. P. Choudhary, Impedance spectroscopy of $(Na_{0.5}Bi_{0.5})$ $(Zr_{0.25}Ti_{0.75})O_3$ lead-free ceramic, *J. Alloys Compd.*, 2008, **453**, 325.

45 W. Lu, S. Jiang, D. Zhou and S. Gong, Structural and electrical properties of Ba(Sn,Sb)O3 electroceramics materials, *Sens. Actuators, A*, 2000, **80**, 35–37.

46 M. D. Migahed, N. A. Bakr, M. I. Abdel-Hamid, O. EL-Hannafy and M. El Nimr, *J. Appl. Polym. Sci.*, 1996, **59**, 655–662.

47 R. N. Bhowmik and I. Panneer Muthuselvam, Dielectric properties of magnetic grains in CoFe1.95Ho0.05O4 spinel ferrite, *J. Magn. Magn. Mater.*, 2013, **335**, 64–74.

48 R. Vaish and K. Varma, Dielectric relaxation in $SrLiB_9O_{15}$ glasses, *J. Electrochem. Soc.*, 2009, **156**, 17–21.

49 H. Zhang, Y. Tang, J. Shen, X. Xin and L. Cui, Chen Antisite defects and Mg doping in $LiFePO_4$: a first-principles investigation, *Appl. Phys. A: Mater. Sci. Process.*, 2011, **104**, 529–537.

50 R. Gerhardt, Impedance and dielectric spectroscopy revisited: distinguishing localized relaxation from long-range conductivity, *J. Phys. Chem. Solids*, 1994, **55**, 1491–1506.

51 H. Lammert and A. Heurer, Contributions to the mixed-alkali effect in molecular dynamics simulations of alkali silicate glasses, *Phys. Rev. B: Condens. Matter Mater. Phys.*, 2005, **72**, 214202–214211.

52 Z. J. Liu, X. J. Huang and D. S. Wang, First-principle investigations of N doping in $LiFePO_4$, *Solid State Commun.*, 2008, **147**, 505.

53 R. Berthelot, D. Carlier and C. Delmas, Electrochemical investigation of the P2–$Na_xCoO_2$ phase diagram, *Nat. Mater.*, 2011, **10**, 74–80.

54 H. V. Doan, V. P. Ting and C. R. Bowena, Understanding the AC conductivity and permittivity of trapdoor chabazites for future development of next-generation gas sensors, *Microporous Mesoporous Mater.*, 2018, **260**, 208–216.